scientific reports

Check for updates

OPEN

High photothermal conversion efficiency of RF sputtered Ti_4O_7 Magneli phase thin films and its linear correlation with light absorption capacity

L. Pichon[1], H. Rekik[2], H. Arab[2], P. Drogui[2] & M. A. El Khakani[1]✉

RF-sputtering is used to deposit Ti_4O_7-Magneli-phase films onto various substrates at deposition temperatures (*Ts*) ranging from 25 to 650 °C. Not only the structural, but also electrical conductivity, optical absorbance and photothermal properties of the Ti_4O_7 films are shown to change significantly with *Ts*. A *Ts* of 500 °C is pointed out as the optimal temperature that yields highly-crystalized pure-Ti_4O_7-Magneli phase with a densely-packed morphology and a conductivity as high as 740 S/cm. The Ti_4O_7 films deposited at *Ts* = 450–500 °C also exhibited the highest optical absorption over all the broad (200–1500) nm range. The absorbed sunlight (AM1.5) was efficiently converted into heat by raising the temperature of the Ti_4O_7 films up to ~ 54 °C. Thus, the external photothermal efficiency (η_{ext}) of the Ti_4O_7 films, was found to be as high as ~ 74%. This is the highest η_{ext} reported so far for sputtered-Ti_4O_7 coatings (just ~ 450 nm-thick), highlighting their significant potential for photothermal applications such as desalination, deicing and/or smart windows. Finally, the η_{ext} of the Ti_4O_7 coatings is demonstrated, for the first time, to be linearly correlated to their integrated light absorption coefficient. This fundamental relationship paves the way towards the design and optimization of highly efficient solar-thermal conversion devices.

Keywords Magneli-phase coatings, Ti_4O_7 thin films, Sputtering, Ultra-broadband absorption, Photothermal conversion

For many decades, titanium dioxide (TiO_2) based materials have been the champion candidates for efficient photocatalysis and/or electrocatalysis[1–6]. Due to its strong photoabsorbance in the UV, chemical stability, high oxidative capacity, and affordability, TiO_2 has been widely used for various applications such as solar energy conversion[7,8], self-photocleaning[9], gas sensing[10], anode for hydrogen production[11,12] or water decontamination[13]. To further extend the photosensitivity of TiO_2 to the visible range, its doping/codoping with appropriate elements (such as N and W) has been shown to be very effective to narrow its bandgap to the visible range and use it successfully for the photodegradation of persistent contaminants in water under sunlight illumination[5,14]. Another approach for sensitizing this photocatalyst material is to prepare TiO_{2-x} sub-oxides with oxygen vacancies[15]. In fact, when there are sufficient oxygen vacancies in the titanium dioxide lattice, new phases can form. Those phases are known under the generic term of Magneli phases, which are basically sub-stoichiometric titanium dioxide obeying the Ti_nO_{2n-1} composition (with $3 \leq n \leq 10$)[16,17]. These Ti_nO_{2n-1} Magneli phase materials exhibit a combination of outstanding properties, such as excellent corrosion resistance, high chemical stability, and astonishingly good electrical conductivity[18,19]. In fact, unlike the semiconducting/insulating behavior of TiO_2 (with a bandgap of 3.0-3.2 eV), the Magneli phases are known for their pseudo-metallic conductivity, with electrical conductivity reaching up to several hundreds of S/cm, particularly for the most conductive Ti_4O_7 composition[20–25].

Thus, Ti_4O_7 arises as the most suitable anode material for different electro-oxidation-based applications, including water decontamination[26–28] or hydrogen production[29,30]. Despite the popularity and attractiveness of Ti_4O_7 Magneli-phase material in the electro-oxidation field, its photothermal properties under solar illumination

[1]Centre Énergie, Matériaux Télécommunications, Institut National de la Recherche Scientifique, 1650, Blvd, Lionel–Boulet, Varennes, QC J3X-1P7, Canada. [2]Centre-Eau Terre Environnement, Institut National de la Recherche Scientifique, 490, Rue de la Couronne, Quebec G1K 9A9, Canada. ✉email: m.a.elkhakani@inrs.ca

have been rather less investigated. Compared to the others photothermal materials (PTMs), transition metal oxides (TMOs) are less expensive than plasmonic metals or complex carbon-based materials and more stable than organic polymers. As a matter of fact, the potential of TMOs based materials for photothermal applications has been documented[31–34]. Among the most attractive TMOs, Fe_3O_4[35,36], black TiO_2[37–39], Ti_2O_3 nanoparticles[40] and Ti_4O_7 nanofibers or nanoparticles[34,41] stand out by their high light-to-heat photoconversion efficiencies, making them highly attractive for water desalination or steam production[34]. For instance, Wang et al. have shown that the addition of Ti_4O_7 nanoparticles (of only 10 wt%) to magnesium nitrate hexahydrate (MNH) phase-change material significantly improved the absorption capacity of the resulting (MNH/Ti_4O_7) composite and consequently its photothermal conversion efficiency[41].

While Ti_4O_7 is known for its high capacity to absorb light[42], it has been mostly used under its powdered form as an additive to produce various hybrid materials (such as fibrous membranes[34], phase-change composites[41], or as microencapsulants[42]) with improved photothermal properties. Under their powdered form, the Magneli phase materials are generally synthetized via the reduction of rutile-TiO_2 powder at high temperatures (in the 800–1150 °C range)[28,43–47]. Several reducing agents can be used, including metals (like Ti[22], and Zr[48]) or gases (such as NH_3[49] or the most widely used H_2[44,50,51]). However, the resulting material generally consists of a mixture of different titanium sub-oxides (TiO_x) phases, making thus the production of a pure Magneli single phase quite challenging. Moreover, the reduction route requires long processing times, high annealing temperatures, and the use of gases requiring particular caution and/or involving safety issues[49,52,53]. It is also worth noting that during the thermal reduction-based synthesis of Ti_nO_{2n-1} powders at high temperatures, the grains/particles tend to grow and agglomerate, making it difficult to control the nanostructure and effective surface of the resulting material (a key issue for electrode applications and rightly so[47,54]). Generally, the produced Magneli-phase powders are pressed to form pellets, which are subsequently used as electrodes in electrochemical applications[26,28,44,55–59].

An interesting alternative to the powdered form and its above-highlighted limitations is the use of plasma-based physical vapor deposition (PVD) methods to produce dense Ti_4O_7 thin film coatings with more flexibility and process latitude. Thus, not only the structure and properties but also the thickness and morphology of the Ti_4O_7 films can be fairly controlled, regardless of the nature of the substrate to be coated. Moreover, the thermal budget for the plasma based synthesis of Magneli phase films is much lower than in classical thermal processing because part of the energy is supplied under an electromagnetic form. The relatively low processing temperatures offer the advantage of preserving the mechanical strength and corrosion resistance of the underlying metallic substrates. So far, several studies have been reported on the deposition of oxygen-deficient TiO_x films via the reactive sputtering of a pure metallic titanium target, while varying the $[O_2]/[Ar]$ flow rate ratio inside the sputtering chamber[60–62]. Thus, several mixed TiO_x phases (including TiO, Ti_2O_3, Ti_4O_7 and TiO_2) films were obtained depending on the O_2 proportion in the plasma carrier gas and/or the deposition temperature. Most of those studies focused on the sputter-deposition of either ultrathin TiO_x films (few 10s of nm-thick) onto various metal electrodes for resistive switching devices[63–65] or relatively thicker coatings (few 100s nm-thick) intended for mechanical or photocatalytic applications[62,66,67]. However, none of those reactive sputtering based processes was reported to produce pure-phase-Ti_4O_7 films. The investigation of the photothermal properties of such sputtered pure-Ti_4O_7 films has also not been reported so far.

Here, we propose an original and direct approach based on the use of a pure Ti_4O_7 target as a source material for the RF-sputter deposition of the Magneli-Ti_4O_7 films under Argon plasma carrier gas without resourcing to any reactive (reducing/oxidizing) background gas. Thus, in this study, we focused on the effect of the substrate deposition temperature (T_s) on the structural, morphological, electrical, optical and photothermal properties of the RF-sputter deposited Ti_4O_7 thin films. By varying T_s in the 25–650 °C temperature range, we demonstrate that single-phase Ti_4O_7 films with high crystalline quality, excellent electrical conductivity and high photothermal efficiency can be obtained at moderate deposition temperatures in the 450–500 °C range. Interestingly, the systematic study of the effect of T_s enabled us to establish, for the first time, that the high photoconversion efficiency of the sputtered-Ti_4O_7 films is linearly correlated to their integrated optical absorbance over the entire (300–1500) nm spectral range. The sputtering process developed here can be used to coat virtually any sort of substrates, widening thereby the range of possible applications for those Magneli-Ti_4O_7 coatings.

Results and discussion

Figure 1a shows the XRD spectra of the Ti_4O_7 films deposited onto Ti substrates as a function of their substrate deposition temperature (T_s). The XRD spectra of the underlying Ti substrate along with that of the Ti_4O_7 target used for the sputter deposition are also included in the figure for reference purposes. It is worth recalling here that the lattice parameters of the various Magneli phases are very close to each other, and some of them even overlap because of their identical triclinic structure[22,49]. More attention is thus required to discriminate between the different Magneli phases by using the XRD peak positions. Nonetheless, there are certain peak positions that can be regarded as fingerprints of the Ti_4O_7 phase. As a matter of fact, the peaks located at $2\theta = 20.7°$, $26.4°$ and $31.7°$, are due to the respective crystallographic plans $\left(10\ \bar{2}\right)$, the $\left(1\ \bar{2}\ 0\right)$ and $\left(10\ \bar{4}\right)$ of Ti_4O_7[34,68,69], and will be used hereafter to qualify for the presence of the Ti_4O_7 phase. These three XRD peaks are also seen to be the most prominent ones in the XRD spectrum of the Ti_4O_7 target source material (bottom blue spectrum of Fig. 1a). Our results clearly show that the films deposited at $T_s = 25$ °C and 300 °C did not exhibit any Ti_4O_7 related diffraction peaks, suggesting that they are amorphous. At $T_s = 450$ °C, 500 °C and 550 °C, the films consist of a well crystallized Ti_4O_7 phase, with its characteristic peaks (at $2\theta = 20.7°$, $26.4°$ and $31.7°$) becoming more intense and narrow as T_s is increased. For $T_s \geq 600$ °C, a phase transition occurs with the appearance of the rutile-TiO_2 phase (at $2\theta = 27.5°$, $36.1°$, $41.3°$, $54.4°$ and 56.7 which becomes dominant at $T_s = 650$ °C.

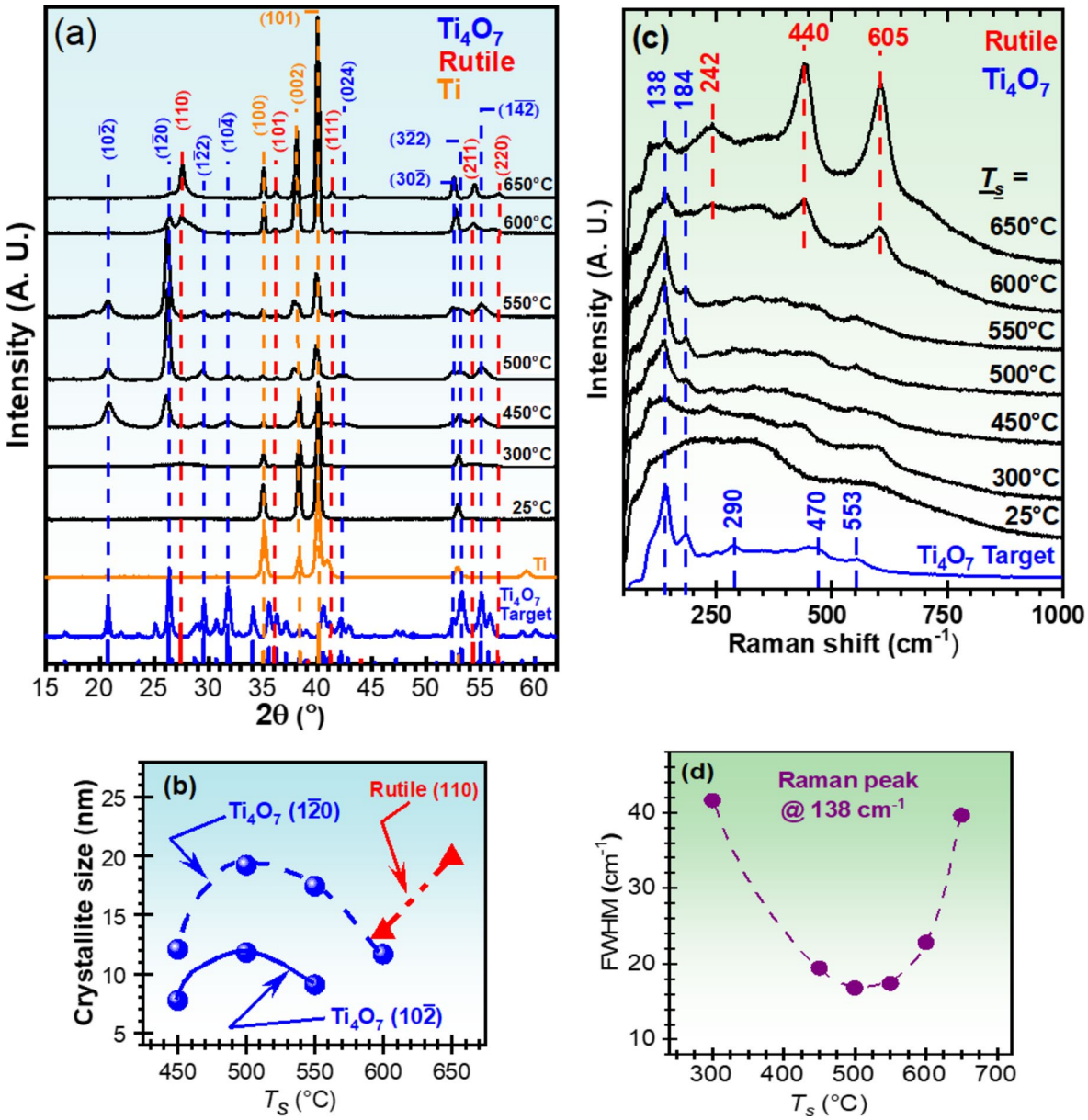

Fig. 1. **(a)** Typical XRD spectra of the sputter-deposited Ti_4O_7 films onto polished Ti substrates, as a function of their T_s. For reference purposes, the peak positions of Ti_4O_7 (in blue, JCPDS-050 0787), of rutile-TiO_2 (in red, JCPDS-004-0551), and of titanium (in orange, JCPDS-005 0682) are also included in the figure; **(b)** T_s dependence of the crystallite size of both Ti_4O_7 and rutile-TiO_2 phases; **(c)** Raman spectra of the sputtered Ti_4O_7 films for the different T_s ranging from 25 to 650 °C. The spectrum of the pure-Ti_4O_7 target (blue line) is also included as a reference; **(d)** T_s dependence of the Full width at half maximum (FWHM) of the 138 cm^{-1} characteristic peak of Ti_4O_7.

By using the Debye-Scherrer formula[70], we have estimated the crystallite size of the $\left(10\,\bar{2}\right)$ and $\left(1\,\bar{2}\,0\right)$ planes of the Ti_4O_7 phase (Fig. 1b). It is found that the size of the Ti_4O_7 crystallites is sensitive to T_s and reaches its maximum value (of ~ 12 and ~ 19 nm, respectively) at $T_s = 500$ °C and then decreases for higher T_s values (≥ 550 °C), where the formation of rutile-TiO_2 starts to take place. These results point out $T_s = 500$ °C as the most favorable substrate temperature for the sputter-deposition of highly crystallized Ti_4O_7 films.

Raman spectroscopy is a very useful technique to use in conjunction with XRD in order to ascertain the presence of the Ti_4O_7 phase (with its characteristic peak located at 138 cm^{-1})[71]. Figure 1c shows the Raman spectra of both the Ti_4O_7 target and the Ti_4O_7 films deposited at different T_s (25–650 °C). It is found that the pure-Ti_4O_7 target exhibits not only the characteristic prominent peak of Ti_4O_7 at 138 cm^{-1}, but also other peaks (184, 290, 470, and 554 cm^{-1}) that can be used to identify the Ti_4O_7 phase. The Ti_4O_7 films deposited at lower temperatures (Ts ≤ 300 °C) exhibit a very broad and diffuse Raman peak covering the (100–400) cm^{-1} range where the Ti_4O_7 Magneli characteristic peaks are expected to appear. This is due to the amorphous state of the

films (as revealed by XRD) where the Ti–O bonds are highly disordered and strongly distorted. As T_s is raised to 300 °C and above, the Ti_4O_7 Raman peaks take shape and become better defined, as a consequence of the temperature induced improvement of structural ordering in the films. Indeed, for 450 °C ≤ T_s ≤ 550 °C, the Ti_4O_7 films are seen to exhibit prominent Raman peaks at 138 and 184 cm^{-1} positions. For the Ti_4O_7 characteristic peak (138 cm^{-1}), the films deposited at T_s = 500 °C exhibited the most intense and narrow one. Figure 1d shows that the full width at half maximum (FWHM) of the 138 cm^{-1} Raman peak significantly decreases and reaches its minimum value at T_s = 500 °C. This peak narrowing is indicative of the higher crystallinity/local ordering of the Ti_4O_7 films deposited at 500 °C. For higher temperatures (T_s ≥ 600 °C), the occurrence of the Ti_4O_7-TiO_2 phase transition is confirmed, as the Raman peaks associated with the rutile-TiO_2 are clearly seen to appear at T_s = 600 °C and become prominent at T_s = 650 °C to the detriment of the vanishing peaks of Ti_4O_7. These Raman results are in accordance with the XRD ones and confirm that T_s = 500 °C is the optimal temperature for obtaining Ti_4O_7 films with the highest crystalline quality.

Figure 2 shows typical SEM images of Ti_4O_7 films deposited at different T_s, namely 25, 500 and 650 °C. The thickness of the sputtered Ti_4O_7 films is typically of ~ 450 nm. The deposition rate of the sputtered Ti_4O_7 films was found to decrease slightly with T_s, from ~ 2.6 ± 0.1 nm/min at T_s = RT to ~ 2.4 ± 0.1 nm/min at T_s = 650 °C. Such a slight decrease of the deposition rate with T_s can result from both crystallization-induced film densification and some possible desorption from the film being deposited at high T_s. On the other hand, the morphology of the sputtered Ti_4O_7 films is found to change with T_s, as illustrated by Fig. 2. At T_s = 25 °C the films are seen to be exhibit a dense featureless and smooth morphology. At the optimal T_s of 500 °C, the morphology of the polycrystalline Ti_4O_7 films remains dense with the appearance of a domed-like fine columns leading to an apparent surface roughness. For high temperatures (T_s ≥ 600 °C), the columnar morphology develops further with the formation of densely packed larger columns and a slightly rougher surface.

In contrast to titanium dioxide (TiO_2), which is a wide bandgap (~ 3.2 eV) semiconductor with an insulating behavior, the Magneli phases are known to be highly conductive, with the Ti_4O_7 phase being the most conductive one with electrical conductivities in the (300–1900) S/cm range, depending on their preparation method and crystalline structure (poly- versus mono-crystalline)[17,20,21,25,72]. Figure 3 shows the T_s dependence of the electrical conductivity of the Ti_4O_7 films (sputter-deposited onto either quartz or silicon substrates). All the Ti_4O_7 films exhibit conductive behavior, with an impressive increase of their conductivity (by more than two orders of magnitude) when their T_s is increased from 25 to 500 °C, reaching up to a value as high as 740 S/cm at the optimal T_s temperature of 500 °C. This conductivity value is quite high for polycrystalline thin films (~ 500 nm-thick), as it falls in the upper range of conductivities quoted for bulk Ti_4O_7[17,25,26,72]. It also compares well with the values generally quoted for graphite (i.e.; 727–1000 S/cm)[54,73,74]. For higher T_s (≥ 550 °C), the conductivity of the Ti_4O_7 films is found to decrease with T_s to a value of ~ 60 S/cm at 650 °C. This is believed to be due to the progressive formation of the less-conductive rutile-TiO_2 phase (as revealed by XRD and Raman results), which takes place to the detriment of the vanishing Ti_4O_7 component of the films.

To characterize the light absorption properties of the Ti_4O_7 films (deposited on quartz), their optical transmittance T(λ) and reflectance R(λ) were systematically measured over the 300–1500 nm spectral range. Figure 4a, b show the T(λ) and R(λ) spectra of the Ti_4O_7 films as a function of their T_s, respectively. For these optical measurements, the thickness of the Ti_4O_7 films (deposited onto optically transparent quartz substrates) was of ~ 130 nm to measure comfortably their optical transmittance. It is seen that the T(λ) of the Ti_4O_7 films is sensitive to their deposition temperature. It overally decreases over the entire spectral range when T_s is increased from 25 to 550 °C (a temperature at which T(λ) reaches its lowest level), then begins to rise back for T_s = 600 °C and 650 °C (Fig. 4a). On the other hand, the reflectance spectra of the Ti_4O_7 films are seen to be quite comparable in the visible for most T_s conditions, but are more scattered in the IR range with the highest reflectances exhibited by the films deposited at T_s ≥ 550 °C. The T(λ) and R(λ) components were used to calculate the absorption coefficient (α (λ)) of our Ti_4O_7 films according to the following equations[75,76]: $\alpha(\lambda) = -\frac{1}{t}\ln\left[\frac{T(\lambda)}{(1-R(\lambda))^2}\right]$, where t is the Ti_4O_7 film thickness. It is worth mentioning here that the Ti_4O_7 films deposited on either silicon, quartz or titanium substrates exhibited the same crystalline structure and bonding states, as confirmed by both

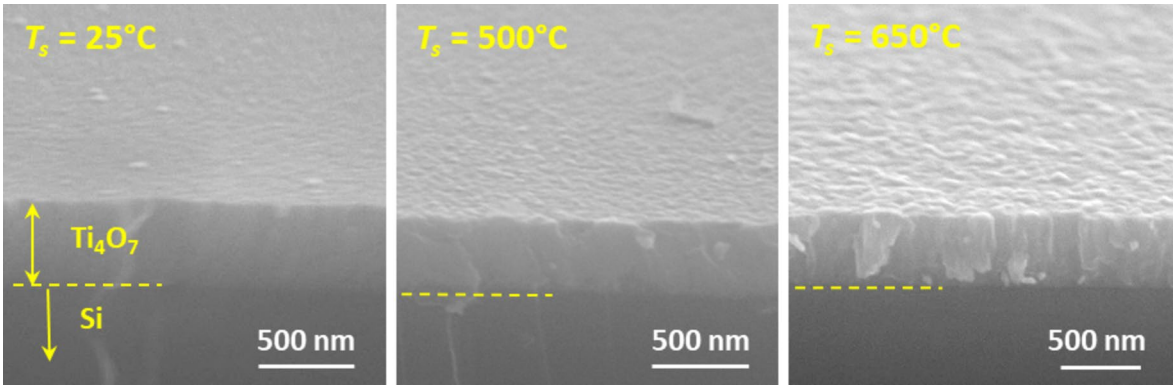

Fig. 2. Typical cross-section SEM images of the sputtered Ti_4O_7 films deposited on silicon substrates at T_s = 25, 500, and 650 °C.

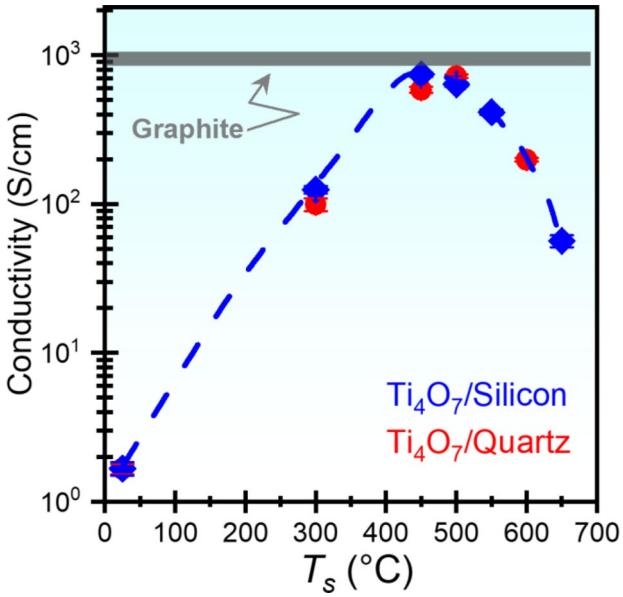

Fig. 3. Electrical conductivity of the Ti_4O_7 films (deposited on both Si and quartz substrates) as a function of their T_s. The conductivity of graphite is also included for comparison.

XRD and Raman spectra (not shown here). Figure 4(c) compares the absorption coefficients , $\alpha(\lambda)$, of the various Ti_4O_7 films deposited at different T_s. It is worth underlying here that expect for the two extreme T_s conditions (namely 25 °C and 650 °C, corresponding to the amorphous and mostly rutile phases, respectively), the sputtered Ti_4O_7 films exhibit strong optical absorption (i.e.; $\alpha(\lambda)$ values in the (0.5–1.7) 10^5 cm^{-1} range) over the broad spectral range of 300–1500 nm. Moreover, the absorption coefficient of the Ti_4O_7 films, over all the entire spectral range, is found to increase significantly as their T_s is raised from 25 to 450 °C (for instance, at a wavelength of 1 µm, the absorption coefficient of the Ti_4O_7 films increased by a factor of 3.3). The maximum of light absorption is exhibited by the Ti_4O_7 films deposited at 450 °C ≤ T_s ≤ 500 °C, where the highly crystallized Ti_4O_7 Magneli phase was formed. For higher T_s (≥ 550 °C), the absorption coefficients progressively diminish going back to $\alpha(\lambda)$ values close to those of the films deposited at T_s = 25 °C. To better qualify the overall light absorption of the Ti_4O_7 films, we calculated their integrated absorption coefficient ($I_{Abs} = \Sigma\alpha(\lambda).\Delta\lambda$, or otherwise the integrated area under the $\alpha(\lambda)$ curve of Fig. 4c) over all the 300–1500 nm spectral range and plotted it as function of T_s. This is a straightforward tool to access easily the light absorption capacity of the Ti_4O_7 films, over the spectral range of interest, without resorting to the spectral emissivity of the films[76] (a physical quantity that is not readily available for Ti_4O_7 films at the wavelengths of interest and certainly not for the temperature of the sample under insolation. Figure 4d clearly shows that the overall optical absorption of the Ti_4O_7 films (as characterized by I_{Abs}) markedly increases (threefolds) when T_s is raised from 25 to 450-500 °C, where it reaches its highest value and then continuously drops back for T_s ≥ 550 °C.

The strong light absorption of sputtered Ti_4O_7 films prompts the evaluation of their capacity to convert the absorbed photons into charges. We have thus investigated the photoconduction properties of the Ti_4O_7 films by performing I–V measurements under both dark and UV lamp illumination (with an irradiance of 32.5 mW/cm^2). Figure 5a shows a typical I-V curve of the Ti_4O_7 films deposited at T_s = 25 °C, where a photocurrent is clearly produced by the films upon their exposure to light. To better compare all the Ti_4O_7 films as a function of their T_s, we have calculated their associated photoresponse (Ph (%), defined as $Ph(\%) = [(I_{Light} - I_{Dark})/I_{Dark}]$ x 100). Figure 5b shows that while the films deposited at T_s = 25 °C exhibited a moderate photoresponse (of ~ 87%), the latter continuously decreases to reach its minimum (of only ~ 15%) at T_s = 500 °C, and then stabilizes around ~ 20% for higher T_s. It is interesting to note that the Ti_4O_7 films deposited at T_s = 500 °C exhibit the lowest photoresponse (Fig. 5(b)) even if their integrated light absorption capacity is the highest (Fig. 4(d)). This suggests that the absorbed photons are not necessarily converted into photocharges that could contribute to enhance the photoconduction of the Ti_4O_7 films. Instead, they might be converted into heat, given the strong capacity of the Ti_4O_7 films to absorb light (and particularly in the IR).

To assess the photo-thermal conversion properties of our sputtered-Ti_4O_7 films, we have calculated their external photothermal conversion efficiency ($\eta_{ext} = Q/q$), which is given by the ratio between their generated heat per surface unit (Q) and the incident photonic power density (q = 1 kW/m^2) delivered by an AM1.5 solar simulator[40,77]. To determine the density of heat (Q) generated by a sample, the latter is exposed to the solar illumination for 15 min while the rise of its temperature is real-time measured by an infrared thermal camera. Thus, the temperature of the sample increases from the ambient temperature (T_{amb}) until it reaches a plateau corresponding to the maximum temperature (T_{max}) of the sample. At this point, a balance is defined between the amount of heat (Q) generated by the illuminated sample and the maximum of heat dissipated to its close surrounding environment (Q_{surr}^{max}), according to the following equation:

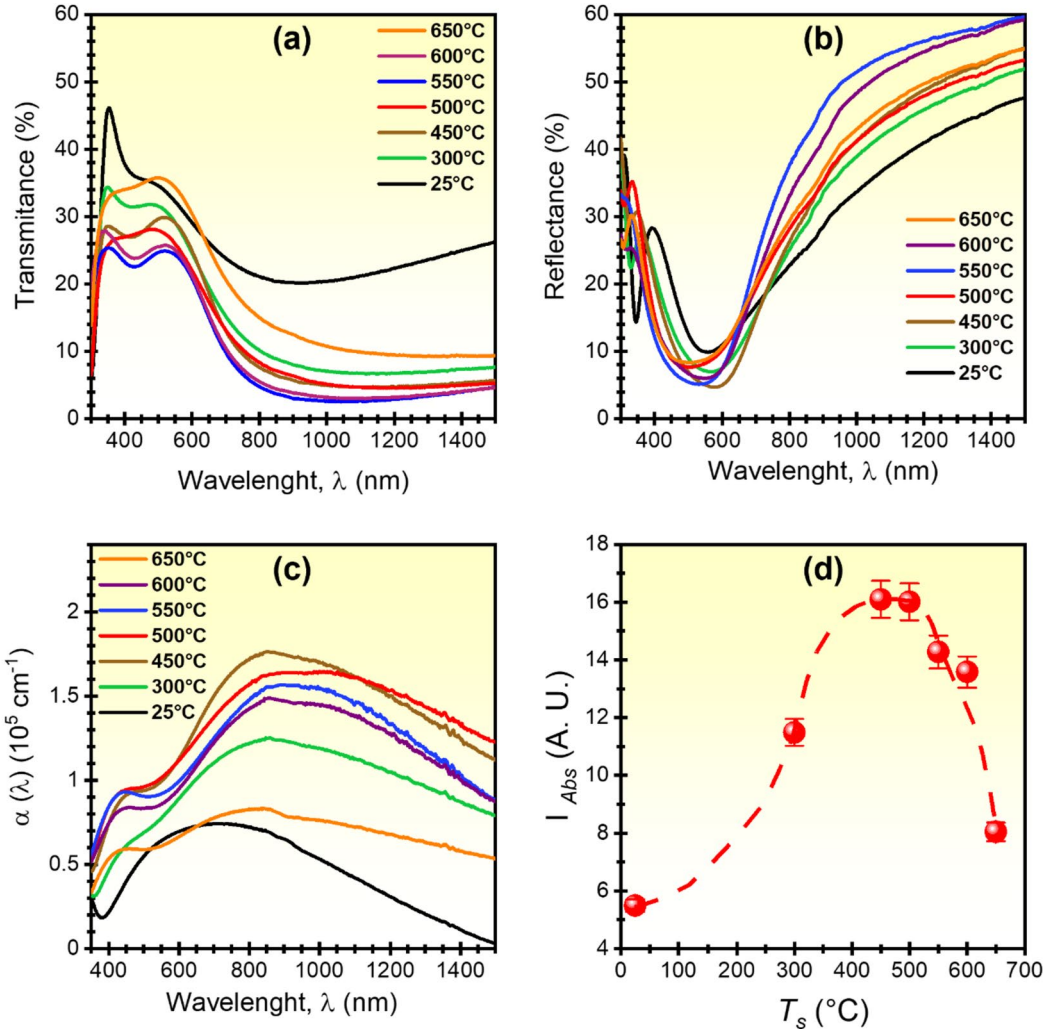

Fig. 4. **(a)** Transmittance; **(b)** Reflectance of the Ti_4O_7 films as a function of T_s; **(c)** Comparison of the absorption coefficients, over the 300–1500 nm spectral range, of the Ti_4O_7 films deposited at different T_s; **(d)** T_s dependence of the integrated absorption coefficient (I_{Abs}) of the Ti_4O_7 films.

$$Q = Q_{surr}^{max} = h \times s \times (T_{max} - T_{surr}^{max}) \tag{1}$$

Where h is the heat transfer coefficient, s is the illuminated surface of the sample, and T_{surr}^{max} is the maximum temperature attained by the surrounding atmosphere of the sample. In a second step, when T_{max} is reached, the solar illumination is turned off and the sample temperature decrease (heat dissipation phase) is tracked until it returns back to ambient. This temperature decay is fitted with the following exponential decay:[40]

$$T(t) = A.e^{(-w \times t)} + B.e^{(-w_{surr} \times t)} + C \tag{2}$$

where $A = T_{max} - B - C$; $B = \frac{w}{w - w_{surr}} \times (T_{surr}^{max} - T_{amb})$; $C = T_{amb} = 25\,\mathrm{C}$, *and* w is the rate of energy loss, which is given by:[40]

$$w = \frac{h \times s}{c_i \times m_i} \tag{3}$$

Where c_i and m_i are the respective heat capacity and mass of the sample. Since our samples consist of a titanium substrate coated with a Ti_4O_7 film, the heat capacities of both materials (0.544 J g^{-1} $°C^{-1}$ and 0.786 J g^{-1} $°C^{-1}$ for Ti[78] and Ti_4O_7[79], respectively) were taken into account in proportion to their actual mass fraction of the sample. The fitting of the temperature decay of the sample by Eq. (2) yields the constant values of A, B, C, w and w_{surr}, enabling thus the calculation of T_{surr}^{max}. In addition, Eq. (3) is used to determine the heat transfer coefficient h of the samples. Finally, by integrating the values of T_{surr}^{max} and h in Eq. (1), the generated heat (Q) can be calculated and the photothermal efficiency (η_{ext}) determined, as above-defined. Figure 6(a) shows

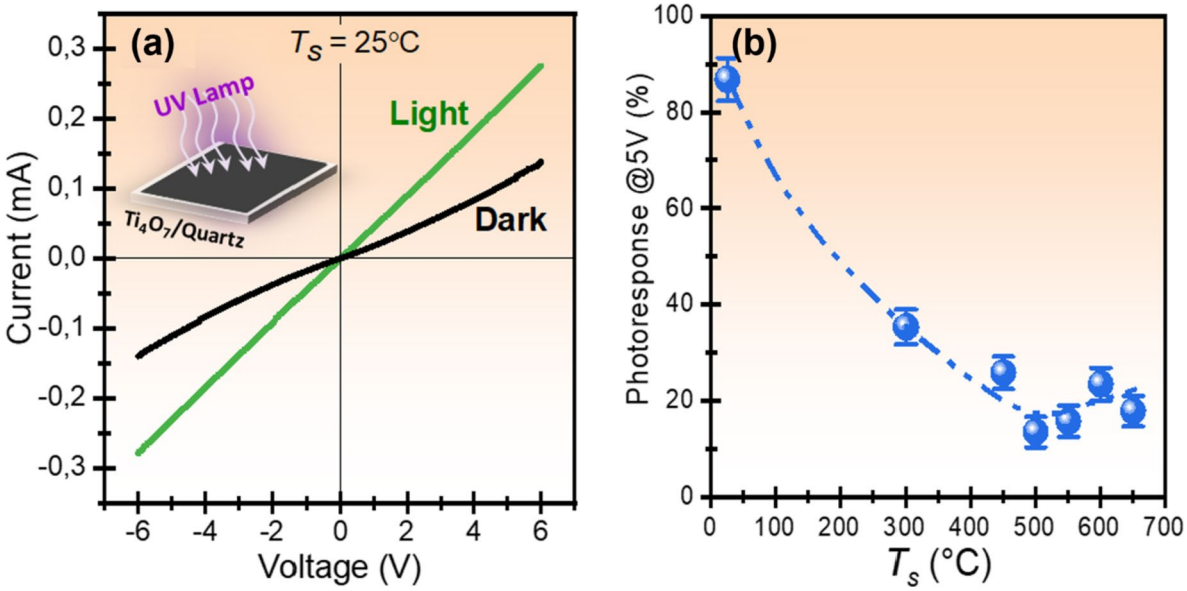

Fig. 5. **(a)** Typical I–V curves of Ti_4O_7 films (deposited at T_s = 25 °C) under dark and light conditions; **(b)** photoresponse of the Ti_4O_7 films as a function of their T_s.

the temperature profiles of the various Ti_4O_7 films (deposited at different T_s) upon their solar illumination. It is clearly seen that the surface temperature of the films rises from T_{amb} = 25 °C until it stabilizes at a maximum temperature (T_{max}) after 900 s of insolation. Firstly, it is worth noting that T_{max} for the bare-Ti substrate (without the Ti_4O_7 coating) reaches a value of only 32.2 ± 0.6 °C. As soon as the Ti substrates are coated with Ti_4O_7 films, their associated T_{max} reaches much higher values. Indeed, T_{max} increases from 41 to 53–54 °C when the deposition temperature of the Ti_4O_7 films is increased from T_s = 25 to T_s = 450–500 °C. It then decreases to 48 °C for the films deposited at T_s = 650 °C. This dependence of T_{max} on the deposition temperature of the Ti_4O_7 films confirms the determining role of the latter in the photothermal conversion process. Interestingly, the photothermal conversion is found to reach its maximum for the Ti_4O_7 films deposited at the optimal T_s of 450–500 °C, where the Ti_4O_7 phase is well crystallized and the highest I_{Abs} is obtained. For T_s = 500 °C, Fig. 6b shows the thermal snapshots of the Ti_4O_7/Ti samples taken by the infrared camera at different illumination times, providing thus a visual evidence of their progressive heating upon illumination. The temperature decays following the shutdown of the illumination at 900s (Fig. 6a) of the different Ti_4O_7/Ti samples (deposited at different T_s) were fitted according to Eq. (2) and their associated photothermal conversion efficiency (η_{ext}) calculated. Figure 6(c) shows the variation of η_{ext} of the Ti_4O_7 films as a function of their T_s. It is seen that η_{ext} is very sensitive to T_s, as it increases from (39.8 ± 1.2) % to as high as (74 ± 2) % when T_s is raised from 25 to = 450–500 °C. For higher T_s values ($\geq$ 550 °C), η_{ext} drops to reach an η_{ext} value of 43.5 ± 1.3% at T_s = 650 °C. All the η_{ext} values exhibited by the Ti_4O_7/Ti samples are significantly higher than that of the bare-Ti substrates (of ~ 18%; see Fig. 6c), confirming the prominent contribution of the Ti_4O_7 coating in the photothermal conversion of the samples. Achieving an η_{ext} as high as ~ 74% by simply coating standard Ti metal substrates by a thin layer (of only ~ 450 nm) of Ti_4O_7 is highly interesting for efficient solar–thermal conversion device applications. The presence of the underlying Ti substrates might have nonetheless lowered the overall photo-thermal conversion performance of the samples, as a part of the heat generated by the Ti_4O_7 coating can be dissipated more easily through the metallic Ti substrates.

In overall, our results suggest that the high-crystallinity of the Ti_4O_7 phase along with its associated high capacity to absorb light are key for an efficient photothermal conversion. By comparing the T_s dependence of both η_{ext} and I_{Abs} (Figs. 4d and 6c, respectively), it strikingly appears that both variations are very similar (i.e.; bell-shaped with their top around T_s = 450–500 °C), suggesting a strong correlation between these two quantities. In fact, this correlation is better evidenced in Fig. 7, where η_{ext} is cross-plotted against I_{Abs}. We were thus able to establish a linear relationship between η_{ext} and I_{Abs}. This clearly demonstrates, for the first time, that the photothermal conversion efficiency (η_{ext}) of the sputtered Ti_4O_7 films linearly scales with their integrated optical absorption coefficient (I_{Abs}). It also provides evidence that there is a direct conversion of the photons absorbed by the Ti_4O_7/Ti samples into heat.

We can thus conclude that the ability to improve the optical absorbance of the Ti_4O_7 films (through surface roughening for example) has the potential to increase further their photothermal conversion efficiency. An extrapolation of the linear relationship established in Fig. 7 suggests that an increase of the optical absorption of the Ti_4O_7 films (by increasing their I_{Abs} by ~ 20%) would lead to an η_{ext} value as high as ~ 95%.

Conclusion

We have successfully developed a magnetron sputtering process for the deposition of Ti_4O_7 thin film coatings onto various substrates. By systematically varying the substrate temperature from 25 to 650 °C, we were able

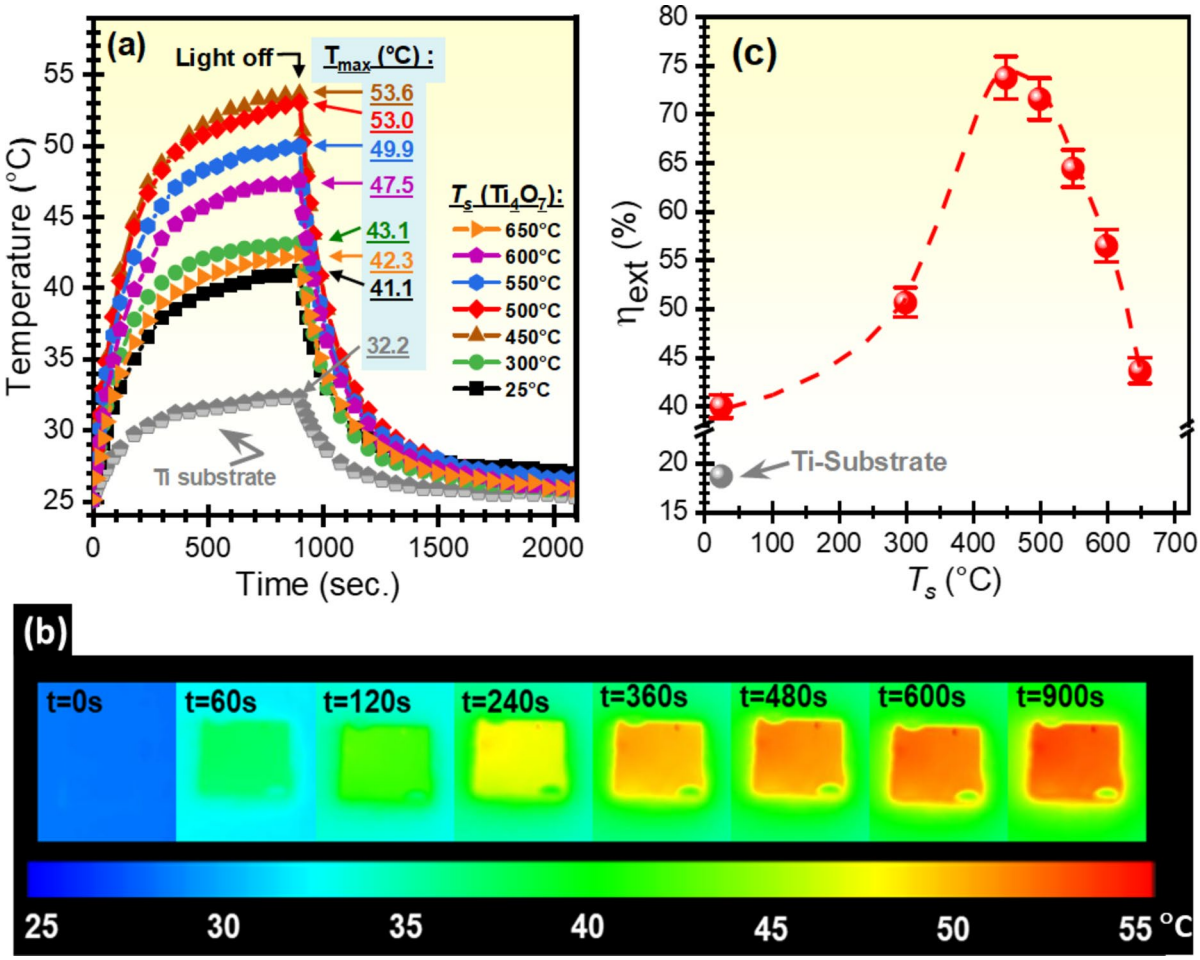

Fig. 6. **(a)** Temperature profiles of the Ti_4O_7 films, deposited at different T_s (the solar simulator was lighted on for 900 s and then shutdown). The maximum temperatures (T_{max}) reached by the samples following their insolation are indicated in light blue box; **(b)** Thermal images of the Ti_4O_7/Ti sample, coated at T_s = 500 °C, taken at different elapsing times (from t = 0 to 900 s); The actual size of the samples is 1″ x 1″; **(c)** External photothermal conversion efficiency (η_{ext}) of the Ti_4O_7 films as a function of their T_s.

to identify an optimal T_s of 500 °C that yields highly crystallized Ti_4O_7 phase films with a densely packed and uniform columnar morphology. At the optimal T_s = 500 °C, not only the Ti_4O_7 crystallite size was found to reach its maximum size of 20 nm, but the Ti_4O_7 films also exhibited their highest electrical conductivity (~ 740 S/cm). For higher T_s (≥ 500 °C), the electrical conductivity of the Ti_4O_7 films starts to drop and reaches ~ 60 S/cm at T_s = 650 °C as a result of a progressive phase transition from Magneli-Ti_4O_7 towards rutile-TiO_2. On the other hand, the light absorption capacity (i.e.; I_{Abs}) of the Ti_4O_7 films is found to be very sensitive to their T_s and reaches its maximum for T_s in the 450–500 °C range. This strong light absorption was shown to be converted efficiently into heat. Indeed, the Ti_4O_7 films deposited at the optimal T_s of 450–500 °C exhibited an external photothermal conversion efficiency as high as ~ 74%. This is an outstanding performance considering the fact that the Ti_4O_7 coatings are deposited onto more heat-dissipating Ti substrates. Interestingly, our results have revealed a striking similarity of the T_s dependence of both η_{ext} and I_{Abs}. This enabled us to establish, for the first time, a linear correlation between the photothermal conversion efficiency of the Ti_4O_7 films and their integrated optical absorbance. This fundamental relationship sets a relatively simple pathway towards the design and optimization of highly efficient solar–thermal conversion devices. Accordingly, it is expected to achieve η_{ext} values of ~ 95% by simply increasing the light absorption of the Ti_4O_7 (by ~ 20%) through, for example, the increase of their surface area. Finally, since sputtering is a well implemented technique in the industrial world with great capacity for large-area coatings and throughput, this work paves the way for the integration of sputtered-Ti_4O_7 coatings into real photothermal devices intended for sustainable water heating, energy storage or water desalination.

Methods

The Ti_4O_7 thin films were deposited using an RF (13.56 MHz) magnetron sputtering system and a Ti_4O_7 target (99.95% pure) at a power density of 7 W/cm^2 and a bias voltage of – 30 V applied on the substrates. Prior to the sputter-deposition, the chamber is first cryo-pumped to a base pressure of ~ 3×10^{-8} Torr. Then, a high-purity

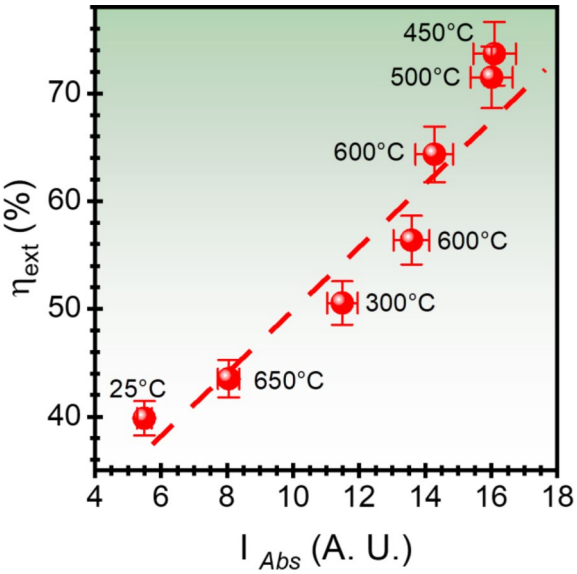

Fig. 7. Linear relationship between the η_{ext} of the Ti_4O_7 films and their integrated optical absorption coefficients (I_{Abs}).

(99.999%) argon gas carrier is injected at a constant flow of 10 sccm to maintain a constant residual pressure of 1.5 mTorr. The substrates to be coated are mechanically attached on the 6″-diam. substrate holder positioned at 20 cm from the target. The substrate holder can be heated from its backside by an array of quartz lamps, allowing to control the actual substrate temperature (T_s) from 25 to 650 °C. Before placing the substrates on the rotating holder, they were cleaned with acetone, isopropanol, rinsed with deionized water and dried by a N_2 jet. The Ti_4O_7 films were concomitantly deposited (in a sputter-up scheme) onto the following substrates: mirror-polished and Si (100), quartz, and pre-etched titanium (of a size of 1″x1″, and 0.02″ thickness). While the Ti_4O_7 deposited onto quartz substrates were mainly used for optical and electrical measurements (because of the optical transparency and insulating character of quartz), those deposited onto silicon were used for SEM observations, and finally those deposited on Ti were used for XRD, Raman and photothermal characterizations. The Ti substrates were prepared by chemically etching their surface for one hour in a 10% (w/v) oxalic acid bath maintained at 90 °C. After their etching, the Ti substrates were cleaned by a standard cleaning procedure (acetone and isopropanol degreasing followed by de-ionized water rinsing) and dried by a N_2 jet. Before starting their coating in the sputtering chamber, the surface of the substrates was in-situ cleaned by subjecting it to a gentle RF argon-plasma (at 20 mW/cm^2 and a resulting bias of − 70 V). The target was also sputter-cleaned by lighting up the plasma for 20 min while keeping the gun shutter closed to shield the substrates. The thickness of the Ti_4O_7 films was in situ monitored by using a calibrated quartz-crystal microbalance. Scanning Electron Microscope (SEM, Tescan Vega 3 LMH) was also used afterwards to *ex-situ* measure the thickness of the films and characterize their morphology. X-ray diffraction (XRD) was employed to determine the crystalline structure of the Ti_4O_7 films deposited onto Ti substrates, as a function of their deposition temperature. The XRD spectra were acquired by using a PANalytical X-Pert-Pro system with a Cu-Kα source (λ = 1.5418 Å) at an incident grazing angle of 1.5°. Raman spectroscopy was also used to characterize the local environments of the Ti_4O_7 films by means of a Renishaw Raman spectrometer (inVia Reflex) using a 50 mW 532-nm-laser source (with an energy filter of 10% and a spot size of ~ 1.5 µm at x50 magnification). The electrical resistivity of the Ti_4O_7 films was systematically measured, as a function of T_s, by means of a four-point Probe testing system (Lucas Lab, S-302). The optical transmittance of the Ti_4O_7 films was characterized with a UV-Vis-NIR spectrophotometer (Perkin Elmer, Lambda 750) equipped with an integrating sphere. Finally, the photothermal properties of our Ti_4O_7 films (deposited onto etched-Ti substrates) were evaluated by placing them at a distance of 15 cm from the simulated sunlight source (AM1.5, 1 kW/m^2). To avoid any heat loss by conduction from the back side of the irradiated sample, the latter was purposely suspended in air by a tiny ceramic frame with solely 4 small point contacts (mm size) at the corners. As such, the heat loss by conduction can be definitely neglected. The heat loss by radiation can also be ruled out as the temperatures reached by the sun irradiated samples remain relatively low (≤ 55 °C). Thus, the real-time temperature evolution of the Ti_4O_7/Ti films (under insolation and after shutting down the illumination) was measured by means of an infrared thermal camera (FLIR, T450sc, with a resolution of 320 × 240 pixels, a thermal sensitivity < 0.03 °C, a temperature range of − 20 to 650 °C). For the IR-camera measurements, we have used an averaged emissivity (ε) value of 0.9 for all the films. This average emissivity (ε) value was chosen after measuring the emissivity values (ε = 1-R, where R is the reflectance measured by FTIR[76,80]) of the sputtered Ti_4O_7 films, over all the (2.5–18) µm IR range, for all the deposition temperatures. In fact, for all the deposition temperatures, the emissivity of our sputtered-Ti_4O_7 films was found to decrease slightly from 0.98 to 0.82 when the IR wavelength is increased from 2.5 to 18 µm. Thus, for practical reasons, we used an averaged fixed value of 0.9 for all the samples. By changing the emissivity of the best performing films

(deposited at T_s = 450 °C) from 0.85 to 0.95, we found that the uncertainty on η_{ext} (obtained at ε = 0.9) is of ± 2.4%. Such an uncertainty is well accounted for in the error bars of Fig. 6c.

Data availability

The data that support the findings of this study are available from the corresponding author (m.a.elkhakani@inrs.ca) upon reasonable request.

Received: 23 July 2024; Accepted: 2 December 2024
Published online: 28 December 2024

References

1. Fujishima, A. & Honda, K. Electrochemical photolysis of water at a semiconductor electrode. *Nature* **238**, 37–38 (1972).
2. Hashimoto, K., Irie, H. & Fujishima, A. TiO_2 photocatalysis: a historical overview and future prospects. *Jpn J. Appl. Phys.* **44**, 8269–8285 (2005).
3. Daghrir, R., Drogui, P., Delegan, N. & El Khakani, M. A. Electrochemical degradation of chlortetracycline using N-doped Ti/TiO_2 photoanode under sunlight irradiations. *Water Res.* **47**, 6801–6810 (2013).
4. Daghrir, R., Drogui, P., Dimboukou-Mpira, A. & El Khakani, M. A. Photoelectrocatalytic degradation of carbamazepine using Ti/TiO_2 nanostructured electrodes deposited by means of a pulsed laser deposition process. *Chemosphere* **93**, 2756–2766 (2013).
5. Delegan, N., Daghrir, R., Drogui, P. & El Khakani, M. A. Bandgap tailoring of in-situ nitrogen-doped TiO_2 sputtered films intended for electrophotocatalytic applications under solar light. *J. Appl. Phys.* **116**, 153510. https://doi.org/10.1063/1.4898589 (2014).
6. Jiang, L. et al. Near-infrared light responsive TiO_2 for efficient solar energy utilization. *Adv. Funct. Mater.* **32**, 2108977. https://doi.org/10.1002/adfm.202108977 (2021).
7. Lan, Y., Lu, Y. & Ren, Z. Mini review on photocatalysis of titanium dioxide nanoparticles and their solar applications. *Nano Energy* **2**, 1031–1045 (2013).
8. Zhou, C., Xi, Z., Stacchiola, D. J. & Liu, M. Application of ultrathin TiO_2 layers in solar energy conversion devices. *Energy Sci. Eng.* **10**, 1614–1629 (2022).
9. Banerjee, S., Dionysiou, D. D. & Pillai, S. C. Self-cleaning applications of TiO_2 by photo-induced hydrophilicity and photocatalysis. *Appl. Catal. B* **176–177**, 396–428 (2015).
10. Garzella, C., Comini, E., Tempesti, E., Frigeri, C. & Sberveglieri, G. TiO_2 thin films by a novel sol–gel processing for gas sensor applications. *Sens. Actuators* **68**, 189–196 (2000).
11. Chiarello, G. L., Dozzi, M. V. & Selli, E. TiO_2-based materials for photocatalytic hydrogen production. *J. Energy Chem.* **26**, 250–258 (2017).
12. Ni, M., Leung, M. K. H., Leung, D. Y. C. & Sumathy, K. A review and recent developments in photocatalytic water-splitting using TiO_2 for hydrogen production. *Renew. Sustain. Energy Rev.* **11**, 401–425 (2007).
13. Chen, D. et al. Photocatalytic degradation of organic pollutants using TiO_2-based photocatalysts: a review. *J. Clean. Prod.* **268**, 121725. https://doi.org/10.1016/j.jclepro.2020.121725 (2020).
14. Delegan, N. et al. In-situ co-doping of sputter-deposited TiO_2:WN films for the development of photoanodes intended for visible-light electro-photocatalytic degradation of emerging pollutants. *J. Appl. Phys.* **123**, 205101. https://doi.org/10.1063/1.5025830 (2018).
15. Liborio, L. & Harrison, N. Thermodynamics of oxygen defective Magnéli phases in rutile: a first-principles study. *Phys. Rev. B* **77**, 104104. https://doi.org/10.1103/PhysRevB.77.104104 (2008).
16. Andersson, S., Bengt, C., Kuylenstierna, U. & Magnéli, A. Phase analysis studies on the titanium-oxygen system. *Acta Chem. Scand.* **11**, 1641–1652 (1957).
17. Walsh, F. C. & Wills, R. G. A. The continuing development of Magnéli phase titanium sub-oxides and Ebonex® electrodes. *Electrochim. Acta* **55**, 6342–6351 (2010).
18. Xu, B., Sohn, H. Y., Mohassab, Y. & Lan, Y. Structures, preparation and applications of titanium suboxides. *RSC Adv.* **6**, 79706–79722 (2016).
19. Chen, X., Liu, L. & Huang, F. Black titanium dioxide (TiO_2) nanomaterials. *Chem. Soc. Rev.* **44**, 1861–1885 (2015).
20. Smith, J. R., Walsh, F. C. & Clarke, R. L. Electrodes based on Magnéli phase titanium oxides, the properties and application of Ebonex materials. *J. Appl. Electrochem.* **28**, 1021–1033 (1998).
21. Bartholomew, R. F. & Frankl, D. R. Electrical properties of some titanium oxides. *Phys. Rev.* **187**, 828–833 (1969).
22. Gusev, A. A., Avvakumov, E. G., Medvedev, A. Z. & Masliy A. I. ceramic electrodes based on Magneli phases of titanium oxides. *Sci. Sinter.* **39**, 51–57 (2007).
23. Gusev, A. A., Avvakumov, E. G. & Vinokurova, O. B. Synthesis of Ti_4O_7 magneli phase using mechanical activation. *Sci. Sinter.* **35**, 141–145 (2003).
24. Liu, H. J., Luo, M. Q., Yang, L. X., Zeng, C. L. & Fu, C. A high strength and conductivity bulk Magnéli phase Ti_4O_7 with superior electrochemical performance. *Ceram. Int.* **48**, 25538–25546 (2022).
25. English, J. T. & Wilkinson, D. P. The superior electrical conductivity and anodic stability of vanadium-doped Ti_4O_7. *J. Electrochem. Soc.* **168**, 103509 (2021).
26. Wang, G., Liu, Y., Ye, J., Lin, Z. & Yang, X. Electrochemical oxidation of methyl orange by a Magneli phase Ti_4O_7 anode. *Chemosphere* **241**, 125084. https://doi.org/10.1016/j.chemosphere.2019.125084 (2020).
27. Li, L., Wang, Y. & Huang, Q. First-principles study of the degradation of perfluorooctanesulfonate and perfluorobutanesulfonate on a Magnéli phase Ti_4O_7 anode. *ACS ES&T Water* **1**, 1737–1744 (2021).
28. Lin, H. et al. Development of macroporous Magnéli phase Ti_4O_7 ceramic materials: as an efficient anode for mineralization of poly- and perfluoroalkyl substances. *Chem. Eng. J.* **354**, 1058–1067 (2018).
29. Wakayama, H. & Yamazaki, K. Low-cost bipolar plates of Ti_4O_7-coated Ti for water electrolysis with polymer electrolyte membranes. *ACS Omega* **6**, 4161–4166 (2021).
30. Wierzbicka, E. et al. Magnéli phases doped with pt for photocatalytic hydrogen evolution. *ACS Appl. Energy Mater.* **2**, 8399–8404 (2019).
31. Gao, M., Zhu, L., Peh, C. K. & Ho, G. W. Solar absorber material and system designs for photothermal water vaporization towards clean water and energy production. *Energy Environ. Sci.* **12**, 841–864 (2019).
32. Tee, S. Y. et al. *In Photothermal Nanomaterials* (eds Ye, E. & Li, Z.) 1–32 (The Royal Society of Chemistry, 2022).
33. Cao, S. et al. Advances in solar evaporator materials for freshwater generation. *J. Mater. Chem. A* **7**, 24092–24123 (2019).
34. Qiu, X., Kong, H., Li, Y., Wang, Q. & Wang, Y. Interface engineering of a Ti_4O_7 nanofibrous membrane for efficient solar-driven evaporation. *ACS Appl. Mater. Interfaces* **14**, 54855–54866 (2022).
35. Song, L., Zhang, X. F., Wang, Z., Zheng, T. & Yao, J. Fe_3O_4/polyvinyl alcohol decorated delignified wood evaporator for continuous solar steam generation. *Desalination* **507**, 115024. https://doi.org/10.1016/j.desal.2021.115024 (2021).
36. Liu, H. et al. Microencapsulating n-docosane phase change material into $CaCO_3$/Fe_3O_4 composites for high-efficient utilization of solar photothermal energy. *Renew. Energy* **179**, 47–64 (2021).

37. Zhu, G., Xu, J., Zhao, W. & Huang, F. Constructing black titania with unique nanocage structure for solar desalination. *ACS Appl. Mater. Interfaces* **8**, 31716–31721 (2016).
38. Liu, X. et al. Black titania/graphene oxide nanocomposite films with excellent photothermal property for solar steam generation. *J. Mater. Res.* **33**, 674–684 (2018).
39. Ye, M. et al. Synthesis of black TiO_x nanoparticles by mg reduction of TiO_2 nanocrystals and their application for solar water evaporation. *Adv. Energy Mater.* **7**, 1601811. https://doi.org/10.1002/aenm.201601811 (2017).
40. Wang, J. et al. High-performance photothermal conversion of narrow-bandgap Ti_2O_3 nanoparticles. *Adv. Mater.* **29**, 1603730. https://doi.org/10.1002/adma.201603730 (2017).
41. Wang, H., Ci, E., Li, X. & Li, J. The magnesium nitrate hexahydrate with Ti_4O_7 composite phase change material for photo-thermal conversion and storage. *Sol Energy* **230**, 462–469 (2021).
42. Zhang, Y. et al. Solar-driven phase change microencapsulation with efficient Ti_4O_7 nanoconverter for latent heat storage. *Nano Energy* **53**, 579–586 (2018).
43. Liang, S., Lin, H., Yan, X. & Huang, Q. Electro-oxidation of tetracycline by a Magnéli phase Ti_4O_7 porous anode: Kinetics, products, and toxicity. *Chem. Eng. J.* **332**, 628–636 (2018).
44. You, S. et al. Monolithic porous Magnéli-phase Ti_4O_7 for electro-oxidation treatment of industrial wastewater. *Electrochim. Acta* **214**, 326–335 (2016).
45. Li, X. et al. Magneli phase Ti_4O_7 electrode for oxygen reduction reaction and its implication for zinc-air rechargeable batteries. *Electrochim. Acta* **55**, 5891–5898 (2010).
46. Geng, P., Su, J., Miles, C., Comninellis, C. & Chen, G. Highly-ordered Magnéli Ti_4O_7 nanotube arrays as effective anodic material for electro-oxidation. *Electrochim. Acta* **153**, 316–324 (2015).
47. Takimoto, D., Toda, Y., Tominaka, S., Mochizuki, D. & Sugimoto, W. Conductive nanosized Magneli-phase Ti_4O_7 with a core@shell structure. *Inorg. Chem.* **58**, 7062–7068 (2019).
48. Kitada, A. et al. Selective preparation of macroporous monoliths of conductive titanium oxides Ti_nO_{2n-1} (n = 2, 3, 4, 6). *J. Am. Chem. Soc.* **134**, 10894–10898 (2012).
49. Tang, C., Zhou, D. & Zhang, Q. Synthesis and characterization of Magneli phases: reduction of TiO_2 in a decomposed NH_3 atmosphere. *Mater. Lett.* **79**, 42–44 (2012).
50. Han, W. Q. & Zhang, Y. Magnéli phases Ti_nO_{2n-1} nanowires: formation, optical, and transport properties. *Appl. Phys. Lett.* **92**, 203117. https://doi.org/10.1063/1.2937152 (2008).
51. Ioroi, T. et al. Stability of corrosion-resistant Magnéli-phase Ti_4O_7 supported PEMFC catalysts at high potentials. *J. Electrochem. Soc.* **155**, B321–B326 (2008).
52. Ertekin, Z., Pekmez, N. Ö. & Pekmez, K. One-step electrochemical deposition of thin film titanium suboxide in basic titanyl sulfate solution at room temperature. *J. Solid State Electrochem.* **24**, 975–986 (2020).
53. Liu, M. et al. Atom-economic synthesis of Magnéli phase Ti_4O_7 microspheres for improved sulfur cathodes for Li–S batteries. *Nano Energy* **79**, 105428. https://doi.org/10.1016/j.nanoen.2020.105428 (2021).
54. Wang, G., Liu, Y., Ye, J. & Qiu, W. Synthesis, microstructural characterization, and electrochemical performance of novel rod-like Ti_4O_7 powders. *J. Alloys Compd.* **704**, 18–25 (2017).
55. Arif, A. F. et al. Highly conductive nano-sized Magneli phases titanium oxide (TiOx). *Sci. Rep.* **7**. https://doi.org/10.1038/s41598-017-03509-y (2017).
56. Li, X., Liu, Y. & Ye, J. Investigation of fabrication of Ti_4O_7 by carbothermal reduction in argon atmosphere and vacuum. *J. Mater. Sci. Mater. Electron.* **27**, 3683–3692 (2015).
57. Lin, M. H., Bulman, D. M., Remucal, C. K. & Chaplin, B. P. Chlorinated by product formation during the electrochemical advanced oxidation process at Magneli phase Ti_4O_7 electrodes. *Environ. Sci. Technol.* **54**, 12673–12683 (2020).
58. Nayak, S. & Brian, C. Fabrication and characterization of porous, conductive, monolithic Ti_4O_7 electrodes. *Electrochim. Acta* **263**, 299–310 (2018).
59. Radecka, M., Trenczek-Zajac, A., Zakrzewska, K. & Rekas, M. Effect of oxygen nonstoichiometry on photo-electrochemical properties of TiO_{2-x}. *J. Power Sources* **173**, 816–821 (2007).
60. Banakh, O., Schmid, P. E., Sanjinés, R. & Lévy, F. Electrical and optical properties of TiOx thin films deposited by reactive magnetron sputtering. *Surf. Coat. Technol.* **151**, 272–275 (2002).
61. Silva Barros, H. W., Duarte, D. A. & Sagás, J. C. Optical and electrical properties of Ti suboxides grown by reactive grid-assisted magnetron sputtering. *Thin Solid Films* **696**, 137762. https://doi.org/10.1016/j.tsf.2019.137762 (2020).
62. Wong, M. S., Lin, Y. J., Pylnev, M. & Kang, W. Z. Processing, structure and properties of reactively sputtered films of titanium dioxide and suboxides. *Thin Solid Films* **688**, 137351. https://doi.org/10.1016/j.tsf.2019.06.001 (2019).
63. Ko, D. S. et al. Effect of the electrode materials on the resistive switching of Ti_4O_7. *Appl. Phys. Lett.* **101**, 053502. https://doi.org/10.1063/1.4739949 (2012).
64. Bae, Y. C. et al. Oxygen ion drift-induced complementary resistive switching in homo TiOx/TiOy/TiOx and Hetero TiOx/TiON/TiOx triple multilayer frameworks. *Adv. Funct. Mater.* **22**, 709–716 (2011).
65. Hu, R. et al. Investigation of resistive switching mechanisms in Ti/TiOx/Pd-based RRAM devices. *Adv. Electron. Mater.* **8**, 2100827. https://doi.org/10.1002/aelm.202100827 (2021).
66. Zapata-Torres, M. et al. Visible and infrared photocatalytic activity of TiO thin films prepared by reactive sputtering. *Mater. Sci. Semicond. Process.* **40**, 720–726 (2015).
67. Mao, Q. et al. Black TiOx films with photothermal-assisted photocatalytic activity prepared by reactive sputtering. *Materials* **14**, 2508. https://doi.org/10.3390/ma14102508 (2021).
68. Geng, P. & Chen, G. Magnéli Ti_4O_7 modified ceramic membrane for electrically-assisted filtration with antifouling property. *J. Membr. Sci.* **498**, 302–314 (2016).
69. Santos, M. C., Elabd, Y. A., Jing, Y., Chaplin, B. P. & Fang, L. Highly porous Ti_4O_7 reactive electrochemical water filtration membranes fabricated via electrospinning/electrospraying. *AIChE J.* **62**, 508–524 (2016).
70. Hajjaji, A., Gaidi, M., Bessais, B. & El Khakani, M. A. Effect of cr incorporation on the structural and optoelectronic properties of TiO_2:Cr deposited by means of a magnetron co-sputtering process. *Appl. Surf. Sci.* **257**, 10351–10357 (2011).
71. Watanabe, M. Raman spectroscopy of charge-ordered states in Magnéli titanium oxides. *Phys. Status Solidi* **6**, 260–263 (2009).
72. Wang, G., Liu, Y., He, W. & Ye, J. Conduction and sintering mechanism of high electrical conductivity Magnéli phase Ti_4O_7. *Ceram. Int.* **49**, 27117–27125 (2023).
73. Shao, Y., Liu, J., Wang, Y. & Lin, Y. Novel catalyst support materials for PEM fuelcells: current status and future prospects. *J. Mater. Chem.* **19**, 46–59 (2009).
74. Weast, R. C. *Handbook of Chemistry and Physics* 60 edn (CRC, 1986).
75. Grigorov, K. G. et al. Optical and morphological properties of N-doped TiO2 thin films. *Surf. Sci.* **605**, 775–782 (2011).
76. Rinnerbauer, V. et al. Metallic photonic crystal absorber-emitter for efficient spectral control in high-temperature solar thermophotovoltaics. *Adv. Energy Mater.* **4**, 1400334 (2014).
77. Roper, D. K., Ahn, W. & Hoepfner, M. Microscale heat transfer transduced by surface plasmon resonant gold nanoparticles. *J. Phys. Chem.* **111**, 3636–3641 (2007).
78. Bros, H., Michel, M. L. & Castanet, R. Enthalpy and heat capacity of titanium based alloys. *J. Therm. Anal.* **41**, 7–24 (1994).
79. Schlenker, C., Lakkis, S., Coey, J. M. D. & Marezio, M. Heat capacity and metal-insulator transmitions in Ti_4O_7 single crystals. *Phys. Rev. Lett.* **32**, 1318–1321 (1974).

80. Shan, S. et al. Spectral emittance measurements of micro/nanostructures in energy conversion: a review. *Front. Energy* **14**, 482–509 (2020).

Acknowledgements
The authors acknowledge the financial support provided by the Natural Sciences and Engineering Research Council (NSERC) of Canada, the Advanced Materials Research and Innovation Hub of the Québec Province (PRIMA Québec), Sanexen and Rio Tinto Iron and Titanium-Quebec.

Author contributions
All the authors have contributed equally to this MS. They have all reviewed the MS and accepted its submission to SciRep.

Declarations

Competing interests
The authors declare no competing interests.

Additional information
Correspondence and requests for materials should be addressed to M.A.E.K.

Reprints and permissions information is available at www.nature.com/reprints.

Publisher's note Springer Nature remains neutral with regard to jurisdictional claims in published maps and institutional affiliations.